### Research Paper

## Single-Sensor Passive Ranging of Underwater Monopoles Using Near-Field/Far-Field Energy Contrasts

Saeir MAHMOUD\*, Louay SALEH, Ibrahim CHOUAIB

Department of Electronic and Mechanical Systems Higher Institute for Applied Sciences and Technology Damascus, Syria

\*Corresponding Author e-mail: saeir.mahmoud@hiast.edu.sy

Received June 26, 2025; accepted September 26, 2025; published online October 27, 2025.

While acoustic vector sensors (AVS) are well-established for detection and direction-of-arrival (DOA) estimation using co-located pressure and particle motion (PM) measurements, their potential for passive range estimation remains largely unexplored. This paper introduces a novel single-AVS method for passive range estimation to an acoustic monopole source by exploiting the fundamental near-field dominance of PM energy. We derive the frequency and the distance dependent ratio ( $\xi$ ) of kinetic to potential acoustic energy density – a key near-field signature inaccessible to conventional hydrophones. By leveraging simultaneous AVS pressure and PM velocity measurements, our method estimates  $\xi$ , inverts the monopole near-field model to obtain the Helmholtz number, and directly computes the range. Crucially, we demonstrate that PM sensors offer a potential signal-to-noise ratio (SNR) advantage over pressure sensors within the near-field (>7.8 dB). Validation under simulated noise conditions shows accurate range estimation (RMSE <10%) for low-frequency sources (<100 Hz) within 8 m–25 m ranges at 0 dB SNRs, with performance degrading as frequency increases or SNR decreases. Critically, robustness is confirmed using recorded basin noise profiles, overcoming the isotropic Gaussian noise assumption. This technique extends AVS functionality beyond DOA, enabling single-sensor passive ranging without arrays, environmental priors, or reference signals where conventional methods fail.

**Keywords:** monopole source; passive ranging; acoustic vector sensor (AVS); particle motion (PM); near-field acoustics; underwater acoustics; energy ratio; single-sensor localization.



#### 1. Introduction

In underwater environment, the use of electromagnetic waves in detection systems faces significant challenges due to attenuation, scattering, and dispersion (Kaushal, Kaddoum, 2016). However, acoustic detection systems have proven to be more effective. The

widely used SONAR system, which is based on acoustic waves, provides a larger coverage area compared to electromagnetic wave-based systems such as radio frequency (RF) and optical systems (KAUSHAL, KADDOUM, 2016; ELEFTHERAKIS, VICEN-BUENO, 2020) (Table 1). Other techniques, such as magnetic detection systems, may also be employed; however, they are

Table 1. Comparison of different wireless underwater technologies (Kaushal, Kaddoum, 2016).

Parameter	Acoustic	RF	Optical	
Attenuation	$0.1\mathrm{dB/km}$ – $4\mathrm{dB/km}$	$3.5\mathrm{dB/m}$ – $5\mathrm{dB/m}$	$0.39\mathrm{dB/m}$ (ocean) $11\mathrm{dB/m}$ (turbid)	
Speed	$1500\mathrm{m/s}$	$2.3\mathrm{m/s}\times10^8\mathrm{m/s}$	$2.3\mathrm{m/s}\times10^8\mathrm{m/s}$	
Distance	Up to km	≤10 m	≈ 10 m–100 m	
Frequency band	$10\mathrm{kHz}$ – $15\mathrm{kHz}$	$30\mathrm{MHz}300\mathrm{MHz}$	$5\mathrm{Hz}\times10^{14}\mathrm{Hz}$	

limited by the low signature of certain underwater objects (SOLDANI *et al.*, 2022).

SONAR systems are categorized as active or passive (ABRAHAM, 2019). Active systems emit high-energy pulses for echo analysis, enabling precise ranging, at the cost of high-power consumption, ecological impact, and operational expense (HARI *et al.*, 2015; JIN, XU, 2020); conversely, passive systems listen to ambient sounds, providing low-cost, energy-efficient, and environmentally benign surveillance (JIN, XU, 2020).

Acoustic fields arise from pressure fluctuations, modeled as monopoles (pulsating spheres), dipoles (out-of-phase monopole pairs), or higher-order multipoles (KALMIJN, 1988). These generate two measurable components: scalar pressure and the vector PM, aligned with the wave direction in the free far-field (Jansen et al., 2017). The pressure-PM relationship, defined by specific acoustic impedance, is real-valued in the far-field but complex in the near-field (LIN et al., 2021). It is a critical distinction for ranging. Sensors diverge in capturing these: hydrophones measure pressure, while acoustic vector sensors (AVS) capture PM (velocity/acceleration) and optionally pressure (TICHAVSKY et al., 2001).

Single-hydrophone systems detect divers (Cole, 2019; Tu et al., 2020; Korenbaum et al., 2020), ships, and biological sources (FERGUSON et al., 2010) but fail at passive ranging without environmental priors. Hydrophone array enable direction-of-arrival (DOA) estimation via beamforming (Krishnaveni et al., 2013) or cross-correlation (SUTIN et al., 2013) but incur prohibitive cost and deployment complexity. While single AVS advances support DOA estimation (Zhao et al., 2018) and detect sources (YUAN et al., 2022), such as divers (MAHMOUD et al., 2025), air gun or boats (Jansen et al., 2017; 2019), they remain prohibitively expensive (Jansen et al., 2017), and research overwhelmingly focuses on DOA - neglecting passive ranging. Existing ranging techniques such as triangulation (ABRAHAM, 2019), multipath delays (ABRAHAM, 2019; Lohrasbipeydeh et al., 2013; Ferguson et al., 2010), dispersion curves (LI et al., 2023), or matched filter (LIANG et al., 2022) require arrays, environmental knowledge, shallow-water constraints, or reference

The fundamental near-field characteristic of PM (exhibiting  $1/r^2$  decay versus pressure's 1/r decay) remains unexploited for passive monopole ranging. We introduce a novel, the unified AVS framework that mathematically models monopole near-field/far-field signatures and fuses pressure energy, particle kinematics, and frequency-dependent decay profiles to jointly estimate the range and DOA using a single sensor. Our key contribution enables single-sensor passive ranging without arrays, environmental priors, or reference signals.

The structure of this paper is arranged as follows: Sec. 2 outlines the fundamental equations governing the propagation of acoustic signals in the underwater environment; Sec. 3 presents an overview of the sensors employed in the detection and localization process, along with the challenges associated with their utilization. The concepts of near-field and far-field, as well as the relationship between pressure signal and PM signals within each field, are discussed in Sec. 4. Section 5 presents and evaluates our proposed methodology for monopole source ranging. Finally, Sec. 6 concludes the paper by summarizing the key findings and their implications.

#### 2. Underwater acoustic wave propagation

Acoustic wave propagation in underwater environments originates from pressure disturbances at the source, governed by the wave equation under assumptions of a homogeneous, lossless, dispersionless, and unbounded medium (ABRAHAM, 2019):

$$\Delta^2 p - \frac{1}{c} \frac{\partial^2}{\partial t^2} p = 0, \tag{1}$$

where p is the acoustic pressure, c is the sound speed in water, and t is time.

For a monopole point source (this study's model), the pressure at a distance r is

$$p(r,t) = \frac{p_0}{r} \cos(2\pi f t - kr), \qquad (2)$$

where  $p_0$  is the pressure magnitude at 1 m, f is the frequency,  $k = 2\pi f/c$  is the wavenumber.

As the wave propagates, it induces oscillatory motion in water particles. The relationship between pressure and PM is defined by Euler's equation which is given as (LIN *et al.*, 2021):

$$\frac{\mathrm{d}\mathbf{v}}{\mathrm{d}t} = \mathbf{a} = -\frac{\nabla p}{\rho},\tag{3}$$

where  $\rho$  is the water density, **v** is the particle velocity, and **a** is the particle acceleration.

Substituting Eq. (2) in Eq. (3) yields:

$$\mathbf{a}(r) = -i2\pi f \frac{p(r,t)}{\rho c} \left( 1 + \frac{i}{kr} \right) \mathbf{u},\tag{4}$$

where  $\mathbf{u}$  is the radial unit vector in spherical coordinates. And the velocity formula  $\mathbf{v}(r,t)$  is given as

$$\mathbf{v}(r) = -\frac{p(r,t)}{\rho c} \left( 1 + \frac{i}{kr} \right) \mathbf{u}. \tag{5}$$

Another important term is the intensity **I**, representing the power flux per unit area, is the time-average product of pressure and particle velocity

(ABRAHAM, 2019). It is given by the following equation (NEDELEC *et al.*, 2021; HOVEM, 2007):

$$\mathbf{I}(r) = \frac{1}{2\rho c} \frac{p_0^2}{r^2} \mathbf{u}.$$
 (6)

This energy propagates as potential and kinetic energy. While the first corresponds to pressure and is more likely to be measured by hydrophones, the second corresponds to the PM and is more likely to be measured by PM sensors. The formula of potential energy density  $\overline{E}_{\rm pot}$  is given as (NEDELEC *et al.*, 2021):

$$\overline{E}_{\text{pot}} = \frac{1}{2\rho c^2} p_{\text{rms}}^2 = \frac{1}{4\rho c^2} \frac{p_0^2}{r^2},$$
 (7)

where  $p_{\rm rms} = \frac{p_0^2}{\sqrt{2}r}$  is the root-mean-square pressure.

And the formula of kinetic energy density  $\overline{E}_{kin}$  is given as (Nedelec *et al.*, 2021):

$$\overline{E}_{\rm kin} = \frac{\rho}{2} v_{\rm rms}^2 = \frac{1}{4\rho c^2} \frac{p_0^2}{r^2} \left( 1 + \frac{1}{(kr)^2} \right), \tag{8}$$

where  $v_{\rm rms}$  is the root-mean-square PM velocity.

Critically  $\overline{E}_{\rm pot}$  decays solely with distance ( $\propto \frac{1}{r^2}$ ), while  $\overline{E}_{\rm kin}$  exhibits frequency-dependent and distance-dependent decay. This fundamental contrast in energy decay profiles underpins our proposed range-estimation method exploiting the near-field PM dominance.

# 3. Sensors employed for acoustic source detection and localization

Underwater acoustic systems utilize two primary sensor types for detection and localization: pressure sensors (hydrophones) and acoustic vector sensors (AVS). These may be deployed singly or in arrays, with the selection driven by application-specific requirements for precision, cost and environmental constraints.

#### 3.1. Pressure sensors (hydrophones)

Hydrophones convert incident acoustic pressure waves into electrical signals via piezoelectric elements (Nedelectric et al., 2021). Under plane-wave conditions, the pressure p and the particle velocity v relate through the specific acoustic impedance  $z_0 = \rho c$  as following:

$$p = z_0 v. (9)$$

Hydrophones exhibit an omni-directional response when their size is small relative to the wavelength of the acoustic signal of interest. In practice, their frequency response typically ranges from a few hertz to several hundred kilohertz (Abraham, 2019; Saheban, Kordrostami, 2021), making them widely used in underwater detection systems.

#### 3.2. Acoustic vector sensor AVS

AVS captures both pressure and vector PM (velocity/acceleration), enabling DOA estimation. Two implementation approaches exist: the inertial method and the pressure gradient method. The first method utilizes accelerometers or geophones to directly measure the particle acceleration or velocity. This approach contends with practical challenges including suspension system, geometry, and buoyancy (GRAY et al., 2016).

Alternatively, the pressure gradient method derives the particle velocity from spatial pressure differences. For the x-component the Euler equation yields:

$$a_x(0,t) = \int_{\tau=0}^{t} v_x(t) d\tau$$

$$\approx \frac{1}{\rho} \frac{p\left(x + \frac{\Delta x}{2}, t\right) - p\left(x - \frac{\Delta x}{2}, t\right)}{\Delta x}, \quad (10)$$

where  $\Delta x$  is the spacing between the two hydrophones. Multi-axis particle measurements require additional hydrophones (e.g., Silvia et al. (2002) used six sensors). Challenges include optimal spacing, calibration, and bandwidth limitation (Nedelec et al., 2021; Gray et al., 2016).

The PM velocity or acceleration is an oscillatory directional quantity that exhibits 180-degree ambiguity. This ambiguity can be resolved by measuring the acoustic intensity, a non-oscillatory quantity that aligns with the direction of wave propagation (Nedelec et al., 2021). Consequently, incorporating a pressure sensor with a multi-axis velocity or acceleration sensor results in an intensity vector sensor commonly referred to as an intensity probe or is a key component constituting the complete AVS system. Furthermore, the dipole directivity pattern (figure-of-eight response) inherent to PM sensors (Yuan et al., 2022) provides a 4.8 reduction in isotropic ambient noise compared to omnidirectional (Levin et al., 2012).

#### 4. Near-field and far-field contrast

The PM equation, described by Eq. (5), governs acoustic wave propagation and reveals a fundamental contrast between the near-field and far-field regions surrounding a source. This equation comprises two primary terms: the first term  $\frac{p(r,t)}{\rho c}$  represents the propagating acoustic wave (far-field component), while the second term  $\frac{ip(r,t)}{\rho ckr}$  represents the local hydrodynamic flow (near-field component) (Kalmijn, 1988). Regions surrounding a source can be divided into three zones as:

- far-field  $(kr \gg 1)$ : the local flow component becomes negligible compared to the propagating

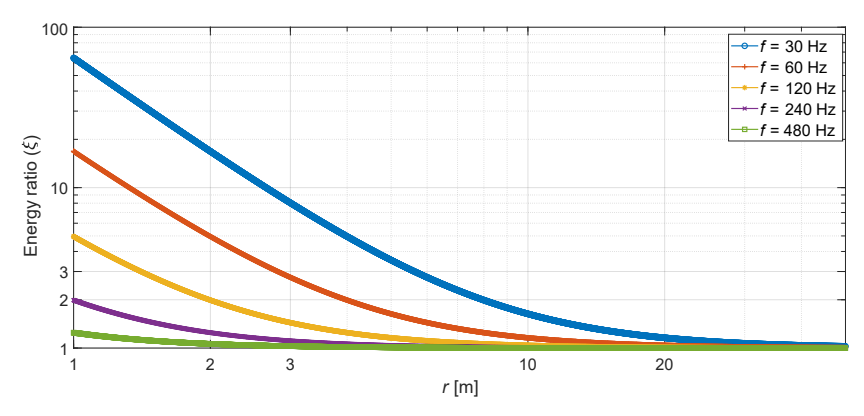


Fig. 1. Variation of energy ratio  $\xi$  with frequency and source distance for an acoustic monopole (logarithmic scale).

wave. Pressure and PM velocity are in phase and related by specific acoustic impedance  $z_0 = \rho c$  as in Eq. (9) and it is real and constant;

- near-field  $(kr \ll 1)$ : the local flow dominates over the propagation wave component. Pressure and PM velocity exhibit a quadrature relationship (90-degree phase difference), and the acoustic impedance becomes complex, frequency-dependent, and varies with distance r and is given as  $z = (p(rt))/(v(rt)) = -i\rho ckr$ . Characteristically, particle velocity decays faster with distance than pressure:
- transition zone  $(kr \approx 1)$ : between these distinct regions lies a transition zone (intermediate zone) where neither component dominates completely.

The Helmholtz number (He = kr), representing the number of wavelengths within the distance r (Jansen et al., 2017), is the key parameter distinguishing these regimes. Since  $k = \frac{2\pi f}{c}$ , He is not solely dependent on the distance r but also on the frequency of the signal. The value of r becomes particularly significant for low frequencies. For example, a 20 Hz source, the nearfield is bounded by a distance r of approximately 12 m (considering  $c = 1500\,\mathrm{m/s}$ ), whereas it is bounded by approximately 1 m for a frequency of 240 Hz.

The magnitude of PM velocity relative to pressure increases as the Helmholtz number decreases (He  $\rightarrow$  0). Consequently, the contribution of kinetic energy to the total energy also increases. This relationship can be observed in the energy equations represented by Eqs. (7) and (8). To quantify this relationship, we defined the energy ratio  $\xi$  as the ratio of time-average kinetic energy density to potential energy density:

$$\xi = \frac{\overline{E}_{\rm kin}}{\overline{E}_{\rm pot}} = \rho^2 c^2 \frac{v_{\rm rms}^2}{p_{\rm rms}^2} = \left(z_0 \frac{v_{\rm rms}}{p_{\rm rms}}\right)^2 = 1 + \frac{1}{(kr)^2}.$$
 (11)

In the far-field,  $p_{\rm rms} = z_0 v_{\rm rms}$ , leading to  $\xi \approx 1$ , indicating equipartition of energy. As He decreases,  $\xi$  increases significantly, reflecting a greater dominance of kinetic energy over potential energy as shown in Fig. 1. This figure graphically represents Eq. (11), it plots  $\xi$ 

against a distance r for selected frequencies on logarithmic axes, clearly showing this increase within the near-field. For instance, at  $r \approx 8\,\mathrm{m}$  and  $f = 30\,\mathrm{Hz}$  ( $kr \approx 1$ ),  $\xi \approx 2$ , meaning that the kinetic energy is nearly twice the potential energy.

This energy distribution difference has implications for the sensor SNR (signal-to-noise ratio). Consider a source producing the potential energy  $E_{\rm pot}$  and the kinetic energy  $E_{\rm kin}$  =  $\xi E_{\rm pot}$  at the sensor location. Under isotropic ambient noise conditions (LEVIN et~al., 2012), the kinematic noise energy  $E_{n_{\rm kin}}$  and potential noise energy  $E_{n_{\rm pot}}$  satisfy  $E_{n_{\rm kin}}$  =  $\frac{1}{3}E_{n_{\rm pot}}$ . Under these assumptions, the SNR at the input of a PM sensor SNR\_v and a pressure sensor SNR\_p satisfy the following equation:

$$\mathrm{SNR}_v = \frac{E_{\mathrm{kin}}}{E_{n_{\mathrm{kin}}}} = 3 \cdot \xi \frac{E_{\mathrm{pot}}}{E_{n_{\mathrm{pot}}}} = 3 \cdot \mathrm{SNR}_p \left( 1 + \frac{1}{(kr)^2} \right). \tag{12}$$

This yields a substantial near-field SNR gain for PM sensors (>7.8 dB at kr < 1). While theoretically significant, practical limitations such as bandwidth constraints in pressure-gradient AVS implementations may mitigate this advantage.

#### 5. Estimating source distance using energy ratio

While conventional AVS applications focus on detection and DOA estimation, this work proposes a novel method for estimating the distance to an acoustic source using a single AVS. This approach exploits the fundamental near-field energy relationship characterized by the ratio  $\xi$  (Eq. (11)), leveraging simultaneous pressure p and PM velocity  $\mathbf{v}(t) = [v_x(t) \ v_y(t) \ v_z(t)]^{\mathrm{T}}$  measurements intrinsic to the AVS.

#### 5.1. Methodological framework

The processing chain (Fig. 2) follows these steps:

1) the AVS outputs four time-domain signals: pressure p(t) and orthogonal velocity components  $v_x(t)$ ,  $v_y(t)$ ,  $v_z(t)$ , related by:

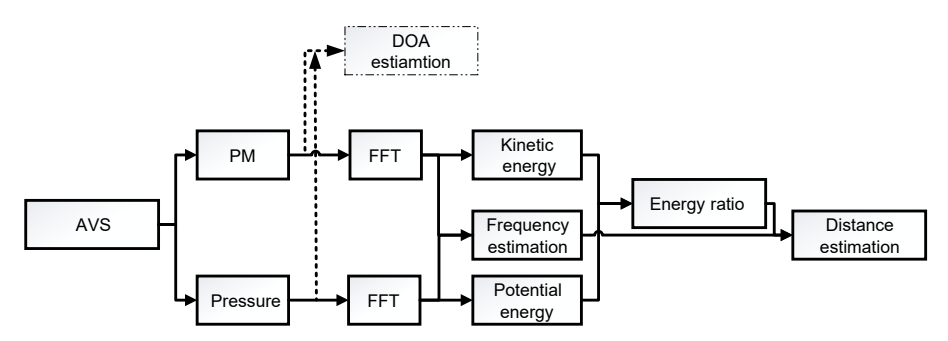


Fig. 2. Proposed processing chain for monopole range estimation using single AVS.

$$\mathbf{v}(t) = \begin{bmatrix} v_x(t) & v_y(t) & v_z(t) \end{bmatrix}^{\mathrm{T}} = -\frac{p(t)}{\rho c} \left( 1 + \frac{i}{k} \right)$$

 $\cdot \left[\cos\theta\cos\phi \quad \sin\theta\cos\phi \quad \sin\phi\right]^{\mathrm{T}}, \quad (13)$ 

where  $\phi$  is the elevation angle and  $\theta$  is the azimuth angle. In the DOA task the estimation of these two angles are done;

2) for a tonal source at frequency  $f_s$ , spectrum estimation is performed using the fast Fourier transform (FFT) which also serves in frequency estimation  $\hat{f_s}$ . The potential energy density estimate is calculated as

$$\widehat{E}_{\text{pot}} = \frac{1}{2\rho c^2} \widehat{p}_{\text{rms}}^2 = \frac{1}{4\rho c^2} |P(f_s)|^2,$$
 (14)

where  $P(f_s)$  denotes the FFT coefficient of p(t) at  $f_s$ .

The kinetic energy density estimate follows as

$$\widehat{E}_{kin} = \frac{\rho}{2} \widehat{v}_{rms}^{2}$$

$$= \frac{\rho}{4} (|V_{x}(f_{s})|^{2} + |V_{y}(f_{s})|^{2} + |V_{z}(f_{s})|^{2}), \quad (15)$$

with  $V_i(f_s)$  representing FFT coefficients of velocity components  $v_i(t)$ , where i corresponds to the Cartesian coordinates x, y, or z, presents this method;

3) the energy ratio  $\xi$  is computed as:

$$\widehat{\xi} = \frac{\widehat{E}_{\text{kin}}}{\widehat{E}_{\text{pot}}}; \tag{16}$$

4) the Helmholtz number He = kr is estimated by inverting the monopole near-field relationship as following:

$$\widehat{He} = \frac{1}{\sqrt{\widehat{\xi} - 1}}; \tag{17}$$

5) finally, the range is derived:

$$\widehat{r} = \frac{c\widehat{He}}{2\pi \widehat{f}_s}.$$
 (18)

For M independent monopole sources emitting distinct, non-overlapping frequencies  $\{f_{s,1},...,f_{s,M}\}$ , the method estimates  $\widehat{E}_k(f_{s,m})$  and  $\widehat{E}_p(f_{s,m})$  across frequencies. Energy at each  $f_{s,m}$  are isolated via frequency-bin selection, and Eqs. (16)–(18) are applied per source to estimate individual ranges  $\widehat{r}_m$ .

#### 5.2. Performance validation

To validate the proposed method, we first performed numerical simulation of monopole radiation in a homogeneous medium. The following assumptions and configurations were adopted:

- sensor model: the AVs modeled as a co-located unit consisting of one omnidirectional pressure sensor and three orthogonal particle velocity sensors. The pressure and velocity components were assumed to be spatially collocated, consistent with an analytical model in Eq. (13);
- medium parameters: a homogeneous, isotropic medium with sound speed  $c = 1500 \,\mathrm{m \cdot s^{-1}}$  and density  $\rho = 1000 \,\mathrm{kg \cdot m^{-3}}$ ;
- source model: a monopole source emitting tonal signals at frequencies  $\{30, 60, 120, 240, 480\}$  Hz. The source is placed at  $(\theta, \phi)$  which are random generated, separated from AVS by a distance  $r \in [1, 100]$  m, as shown in Fig. 3. Multipath and depth-related effects were neglected;
- noise model: independent additive white Gaussian noise (AWGN) was applied to each channel. SNR values tested were -6 dB, 0 dB, and 6 dB per channel.
- computational environment: simulation was implemented in Matlab. 1-second analysis window was used. For each configuration, 1000 Monte Carlo trials were run;
- performance metric: the range estimation error  $\delta_{\rm err}$  was quantified using the relative error defined in Eq. (19):

$$\delta_{\text{err}} (\%) = \begin{cases} 100 \frac{|r - \widehat{r}|}{r} & \xi \ge 1, \\ 100 & \xi < 1. \end{cases}$$
 (19)

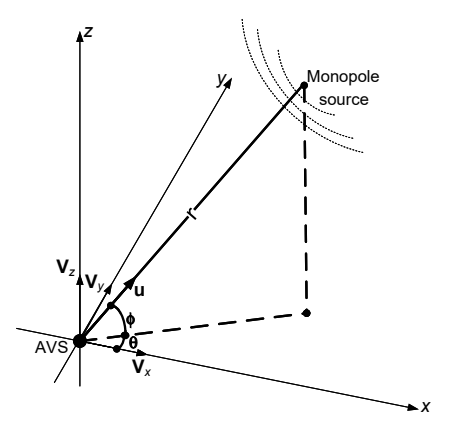


Fig. 3. Geometry of the monopole source relative to AVS. The Cartesian unit vectors  $(\mathbf{V}_x, \mathbf{V}_y, \mathbf{V}_z)$  define the sensor's coordinate frame. The source direction is described by the azimuth  $(\theta)$  and elevation  $(\phi)$  angles, the radial unit vector  $(\mathbf{u})$ , and the radial distance (r).

The resulting RMSE (root mean square error) of  $\delta_{\rm err}$  is calculated and logarithmically presented in

Figs. 4–6, demonstrating the method's range-frequency dependence. Figure 5 shows that estimation with a 10 % error, for SNR = 0 dB, is achieved for distances up to 25 m when dealing with a source emitting 30 Hz frequency signal. This distance decreases to 6.6 m when the source frequency increases to 120 Hz. These results exhibit an enhancement when SNR increases: in Fig. 6, with SNR = 6 dB, the 10 % error is extended to 37 m at 30 Hz. In contrast, when SNR decrease to  $-6\,\mathrm{dB}$  (Fig. 4), the maximum distance decreases to 17 m. Overall, all curves in Fig. 5 will rightward shift with increasing the SNR (Fig. 6), while decreasing SNR causes the curves to shift towards the left (Fig. 4), confirming a strong SNR-frequency dependence.

#### 5.3. Limitations and operational quidelines

The method achieves the highest accuracy where  $kr \lesssim 1$   $(x \gtrsim 2)$  exemplified by <6% error at 30 Hz within 20 m. However, the far-field operation  $kr \gg 1$   $(\xi \approx 1)$  requires impractical SNR (SNR  $\gg 0$  dB).

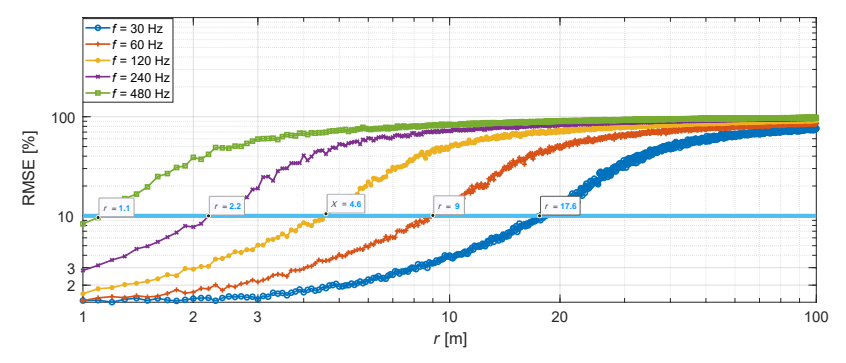


Fig. 4. Range estimation RMSE at SNR =  $-6 \, dB$ .

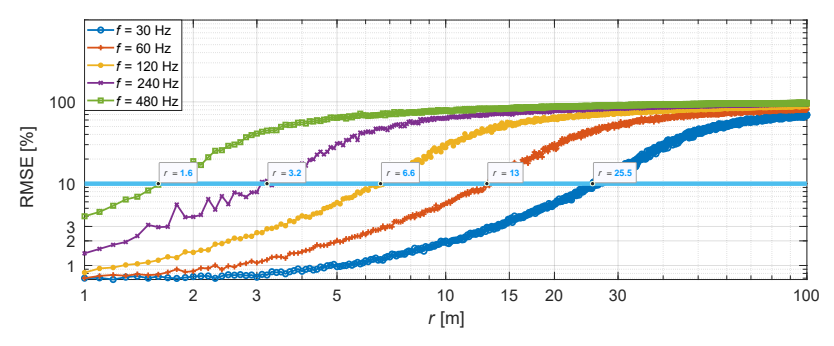


Fig. 5. Range estimation RMSE at SNR =  $0\,\mathrm{dB}$ .

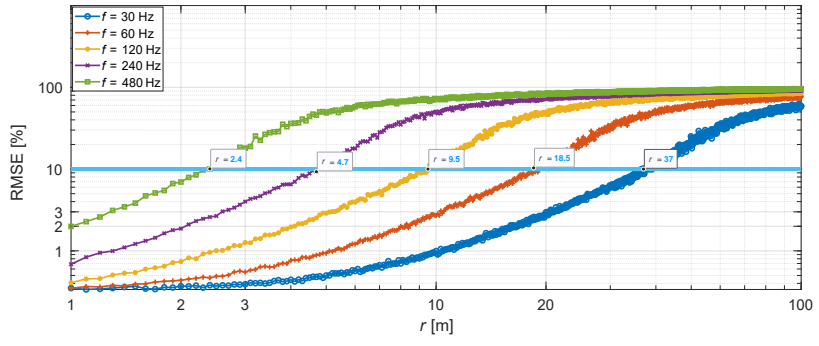


Fig. 6. Range estimation RMSE at  $SNR = 6 \, dB$ .

In high-frequency ( $\geq$  480 Hz) or noisy (SNR  $\ll$  0 dB) environments, it primarily functions as a proximity indicator. Accuracy assumes monopole-like radiation; dipoles/quadrupoles alter the  $\xi$  vs. kr relationship. Additionally, at low frequencies, large wavelengths yield multipath effects in bounded environments, degrading ranging affects this approach.

This technique extends AVS functionality beyond DOA, enabling single-sensor ranging where conventional methods fail – particularly valuable for near-field targets in constrained applications. Operational effectiveness peaks for low-frequency sources (<100 Hz) within  $8\,\mathrm{m}{-}25\,\mathrm{m}$  ranges at  $0\,\mathrm{dB}$  SNR.

## 5.4. Experimental validation with realistic noise profiles

To validate robustness beyond the isotropic additive Gaussian noise assumption used in simulations, experiments employed authentic ambient noise recorded from an operational test basin ( $25\,\mathrm{m}\times15\,\mathrm{m}\times2\,\mathrm{m}$ ) using the AVS configuration characterized in (Mahmoud et al., 2025) (see Fig. 4 for time-series and spectrogram representations).

Analysis of the realistic noise (Fig. 7) revealed the following key characteristics:

- pressure vs. velocity noise: noise in the pressure channel exceeds that in the velocity channels, consistent with its omnidirectional sensitivity;
- distinct self-noise profiles: the inherent self-noise characteristics differ between the pressure sensor and velocity sensor. The isotropic conditions are not satisfied (when calculating the pressure power and velocity power);
- velocity channel coherence: the three orthogonal velocity channels exhibit the same levels and waveforms noise;
- spectral tilt: noise energy decreased significantly with increasing frequency;
- tonal interference: prominent tonal interference was present.

To evaluate range estimation performance, we injected a directional tonal signal into the recorded noise. The amplitude was calibrated to achieve SNR =  $0\,\mathrm{dB}$  when added to the AVS pressure channel noise. The same tonal signal, respecting its DOA, was injected into the velocity channel noise signals. We applied

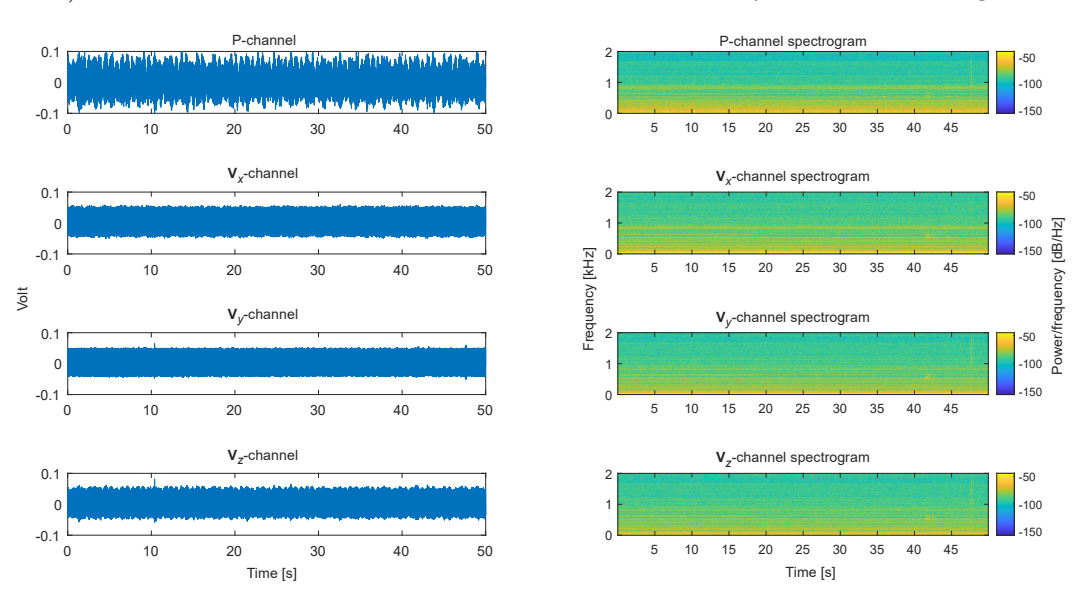


Fig. 7. Measured AVS noise signal.

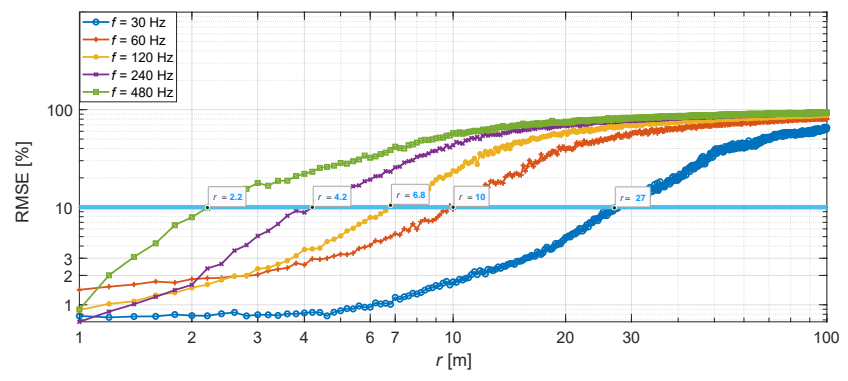


Fig. 8. Range estimation RMSE under realistic ambient noise (SNR = 0 dB).

the proposed algorithm to this combined signal-plusnoise data.

Figure 8 shows estimated range vs true range under realistic noise (SNR =  $0\,\mathrm{dB})$  for representative frequencies. Performance was assessed using 1000 Monte Carlo trials, each employing a different 1-second segment of the recorded noise. The results demonstrate that the proposed algorithm is significantly less affected by realistic noise compared to simulated AWGN conditions. For a 30 Hz tonal signal at a range of 27 m, the RMSE corresponds to less than 10 % relative error. This confirms the method's viability and robustness in nonideal, real-world noise environments, extending beyond the limitations of theoretical AWGN assumptions.

#### 6. Conclusion

This study has established a novel framework for passive monopole source ranging in underwater acoustics using a single AVS. By exploiting the fundamental near-field dominance of PM energy – quantified by the kinetic-to-potential energy density ratio  $(\xi)$  – we demonstrate that AVS measurements enable single-sensor range estimation where conventional hydrophone arrays fail. Key findings reveal:

- 1) PM SNR advantage: PM sensors achieve higher SNR than pressure sensors in the near field  $(kr \lesssim 1)$ , validating the theoretical foundation for our approach;
- 2) accurate passive ranging: the proposed energy-decay method enables passive ranging up to 25 m for 30 Hz sources at 0 dB SNR with <10 % error;
- 3) real-noise robustness: validation using recorded basin noise profiles confirms the method viability despite violating the isotropic noise assumption.

While effective for near-field monopoles, limitations exist: performance degrades at high frequencies due to near-field contraction and in bounded environments where a low-frequency multipath distorts wave propagation. Future work will extend this framework to broadband sources and experimental validation in complex channels. This technique significantly advances passive sonar capabilities, enabling compact, cost-effective solutions for close-range surveillance.

#### Fundings

This research did not receive any specific grant from funding agencies in the public, commercial, or not-for-profit sectors.

#### Conflict of interest

The authors declare that they have no known competing financial interests or personal relationships that could have appeared to influence the work reported in this paper.

#### Data availability statement

The data that support the findings of this study are available from the corresponding author upon reasonable request.

#### AUTHORS' CONTRIBUTIONS

Saier Mahmoud – methodology, software, hardware, writing (primary); Louay Saleh – hardware, supervision, conceptualization, revision; Ibrahim Chouaib – supervision, conceptualization, revising.

#### References

- 1. Abraham D.A. (2019), Underwater Acoustic Signal Processing: Modeling, Detection, and Estimation, Springer.
- Cole A.M. (2019), Automated open circuit scuba diver detection with low cost passive sonar and machine learning, Msc. Thesis, Massachusetts Institute of Technology, Woods Hole Oceanographic Institution, United States.
- 3. Eleftherakis D., Vicen-Bueno R. (2020), Sensors to increase the security of underwater communication cables: A review of underwater monitoring sensors, Sensors, 20(3): 737, https://doi.org/10.3390/s20030737.
- FERGUSON B.G., LO K.W., RODGERS J.D. (2010), Sensing the underwater acoustic environment with a single hydrophone onboard an undersea glider, [in:] OCEANS'10 IEEE Sydney, https://doi.org/10.1109/ OCEANSSYD.2010.5603889.
- Gray M., Rogers P.H., Zeddies D.G. (2016), Acoustic particle motion measurement for bioacousticians: Principles and pitfalls, [in:] Proceedings of Meetings on Acoustics, 27(1): 010022, https://doi.org/10.1121/ 2.0000290.
- HARI V.N., CHITRE M., TOO Y.M., PALLAYIL V. (2015), Robust passive diver detection in shallow ocean, [in:] OCEANS 2015 Genova, https://doi.org/10.1109/OCEANS-Genova.2015.7271656.
- HOVEM J.M. (2007), Underwater acoustics: Propagation, devices and systems, *Journal of Electroceramics*, 19: 339–347, https://doi.org/10.1007/s10832-007-9059-9.
- 8. Jansen H.W., Brouns E., Prior M.K. (2017), Vector sensors and acoustic calibration procedures, TNO report (TNO 2017 R11589).
- 9. Jansen H.W., Prior M.K., Brouns E. (2019), On the conversion between sound pressure and particle motion, [in:] *Proceedings of Meetings on Acoustics*, **37**(1): 070012, https://doi.org/10.1121/2.0001280.
- JIN B., Xu G. (2020), A passive detection method of divers based on deep learning, [in:] *IEEE 3rd Interna*tional Conference on Electronics Technology, pp. 650– 655, https://doi.org/10.1109/ICET49382.2020.9119556.

- KALMIJN Ad.J. (1988), Hydrodynamic and acoustic field detection, [in:] Sensory Biology of Aquatic Animals, pp. 83–130, Springer, https://doi.org/10.1007/ 978-1-4612-3714-3\_4.
- KAUSHAL H., KADDOUM G. (2016), Underwater optical wireless communication, IEEE Access, 4: 1518–1547, https://doi.org/10.1109/ACCESS.2016.2552538.
- 13. Korenbaum V., Kostiv A., Gorovoy S., Dorozhko V., Shiryaev A. (2020), Underwater noises of opencircuit scuba diver, *Archives of Acoustics*, **45**(2): 349– 357, https://doi.org/10.24425/aoa.2020.133155.
- KRISHNAVENI V., KESAVAMURTHY T., B. Aparna (2013), Beamforming for direction-of-arrival (DOA) estimation A survey, *International Journal of Computer Applications*, 61(11): 4–11, https://doi.org/10.5120/9970-4758.
- LEVIN D., HABETS E.A.P., GANNOT S. (2012), Maximum likelihood estimation of direction of arrival using an acoustic vector-sensor, The Journal of the Acoustical Society of America, 131(2): 1240–1248, https://doi.org/10.1121/1.3676699.
- Li X., Chen H., Lu H., Bi X., Mo Y. (2023), A method of underwater sound source range estimation without prior knowledge based on single sensor in shallow water, Frontiers in Physics, 11: 1109220, https://doi.org/ 10.3389/fphy.2023.1109220.
- Liang N., Zhou J., Yang Y. (2022), Single hydrophone passive source range estimation using phase-matched filter, *Journal of Marine Science and Engineering*, 10(7): 866, https://doi.org/10.3390/jmse10070866.
- 18. Lin H., Bengisu T., Mourelatos Z.P. (2021), Lecture Notes on Acoustics and Noise Control, Springer.
- LOHRASBIPEYDEH H., GULLIVER T.A., ZIELINSKI A., DAKIN T. (2013), Single hydrophone passive source range and depth estimation in shallow water, [in:] OCEANS 2013 MTS/IEEE Bergen, https://doi.org/ 10.1109/OCEANS-Bergen.2013.6608042.
- Mahmoud S., Saleh L., Chouaib I. (2025), Experimental results of diver detection in harbor environments using single acoustic vector sensor, *Archives of Acoustics*, 50(2): 173–185, https://doi.org/10.24425/aoa.2025.153663.
- 21. Nedelec S.L. et al. (2021), Best practice guide for underwater particle motion measurement for biological

- applications, Technical report by the University of Exeter for the IOGP Marine Sound and Life Joint Industry Programme, https://www.researchgate.net/publication/356911609.
- 22. Saheban H., Kordrostami Z. (2021), Hydrophones, fundamental features, design considerations, and various structures: A review, *Sensors and Actuators A: Physical*, **329**: 112790, https://doi.org/10.1016/j.sna. 2021.112790.
- 23. SILVIA M.T., RICHARDS R.T. (2002), A theoretical and experimental investigation of low-frequency acoustic vector sensors, [in:] *OCEANS '02 MTS/IEEE*, **3**: 1887–1898, https://doi.org/10.1109/oceans.2002.1191918.
- 24. SOLDANI M., FAGGIONI O., ZUNINO R., CARBONE A., GEMMA M. (2022), The LAMA system: A "smart" magnetometer network for harbour protection, *Journal* of Applied Geophysics, 204: 104743, https://doi.org/ 10.1016/j.jappgeo.2022.104743.
- Sutin A., Salloum H., Delorme M., Sedunov N., Sedunov A., Tsionskiy M. (2013), Stevens passive acoustic system for surface and underwater threat detection, [in:] 2013 IEEE International Conference on Technologies for Homeland Security (HST), pp. 195– 200, https://doi.org/10.1109/THS.2013.6698999.
- TICHAVSKY P., WONG K.T., ZOLTOWSKI M.D. (2001), Near-field/far-field azimuth and elevation angle estimation using a single vector hydrophone, [in:] *IEEE Transactions on Signal Processing*, 49(11): 2498–2510, https://doi.org/10.1109/78.960397.
- 27. Tu Q., Yuan F., Yang W., Cheng E. (2020), An approach for diver passive detection based on the established model of breathing sound emission, *Journal of Marine Science and Engineering*, 8(1): 44, https://doi.org/10.3390/JMSE8010044.
- 28. Yuan M., Wang C., Da L., Li Q. (2022), Signal detection method using a single vector hydrophone in ocean acoustics, *The Journal of the Acoustical Society of America*, **152**(2): 789–798. https://doi.org/10.1121/10.0013219.
- Zhao A., Ma L., Hui J., Zeng C., Bi X. (2018), Open-lake experimental investigation of azimuth angle estimation using a single acoustic vector sensor, *Journal of Sensors*, 2018: 4324902, https://doi.org/10.1155/2018/4324902.